



CHORUS

This is the accepted manuscript made available via CHORUS. The article has been published as:

Appearance of superconductivity at the vacancy order-disorder boundary in $\text{K}_{\{x\}}\text{Fe}_{\{2-y\}}\text{Se}_{\{2\}}$

Chunruo Duan, Junjie Yang, Yang Ren, Sean M. Thomas, and Despina Louca

Phys. Rev. B **97**, 184502 — Published 14 May 2018

DOI: [10.1103/PhysRevB.97.184502](https://doi.org/10.1103/PhysRevB.97.184502)

Appearance of Superconductivity at the vacancy order-disorder boundary in $\text{K}_x\text{Fe}_{2-y}\text{Se}_2$

Chunruo Duan,¹ Junjie Yang,¹ Yang Ren,² Sean M. Thomas,³ and Despina Louca^{*1}

¹*University of Virginia, Charlottesville, VA 22904, USA.*

²*Advanced Photon Source, Argonne National Laboratory, Argonne, Illinois 60439, USA*

³*Los Alamos National Laboratory, Los Alamos, NM 87544*

(Dated: May 4, 2018)

The role of phase separation and the effect of Fe vacancy ordering in the emergence of superconductivity in alkali metal doped iron selenides $\text{A}_x\text{Fe}_{2-y}\text{Se}_2$ ($\text{A} = \text{K}, \text{Rb}, \text{Cs}$) is explored. High energy X-ray diffraction and Monte Carlo simulation were used to investigate the crystal structure of quenched superconducting (SC) and as-grown non-superconducting (NSC) $\text{K}_x\text{Fe}_{2-y}\text{Se}_2$ single crystals. The coexistence of superlattice structures with the in-plane $\sqrt{2} \times \sqrt{2}$ K-vacancy ordering and the $\sqrt{5} \times \sqrt{5}$ Fe-vacancy ordering were observed in both the SC and NSC crystals along side the $I4/mmm$ Fe-vacancy free phase. Moreover, in the SC crystals, an Fe-vacancy disordered phase is additionally proposed to be present. Monte Carlo simulations suggest that it appears at the boundary between the $I4/mmm$ vacancy-free phase and the $I4/m$ vacancy-ordered phases ($\sqrt{5} \times \sqrt{5}$). The vacancy disordered phase is non-magnetic and is most likely the host of superconductivity.

The coexistence and self-organization of multiple phases into complex morphologies provide for an electronic complexity that is at the heart of strongly correlated electron systems¹. In the Fe-based and cuprate superconductors, superconductivity emerges by suppressing the static antiferromagnetic (AFM) order² but spin and charge density fluctuations persist, and are critical in the electron pairing mechanism. Coupled with these fluctuations is a heterogeneous lattice where the spatial interplay between the spin and charge degrees of freedom leads to nanoscale phase separation³. Thus the lattice structure is a signature of the phase separation and it is key to elucidating the symmetry-breaking ground state properties that allow superconductivity to evolve. The $\text{A}_x\text{Fe}_{2-y}\text{Se}_2$ system is a test bed for exploring the very peculiar crystal symmetries that appear because of the close proximity of superconductivity to a magnetic insulating state, leading to a multiphase complex lattice whose precise nature has not been resolved, in spite of many studies. This has been in part due to inconsistent sample chemistry and an intricate vacancy ordering scheme that led to many different proposed crystal phases.

The $\text{A}_x\text{Fe}_{2-y}\text{Se}_2$ ($\text{A} = \text{K}, \text{Rb}, \text{Cs}$) iron selenide superconductor class has been intensely studied⁴ in part due to the Fe-vacancy order and of its role in phase separation that may lead to SC and NSC regions⁵⁻⁹. With vacancies at both the A and Fe sites, a well-known structural transition occurs when the Fe vacancies order at $T_S \sim 580 \text{ K}$ ⁵. Above T_S in the high temperature tetragonal phase with the $I4/mmm$ space group, the vacancies are randomly distributed at both the Fe and A sites. Upon cooling below T_S , a superlattice structure appears due to Fe vacancy order. Several scenarios have been proposed regarding the nature of the microstructure below T_S . In one, the lattice is phase separated into a minority $I4/mmm$ phase which is compressed in-plane and extended out-of-plane in comparison to the high temperature centrosymmetric phase and has no Fe vacancies,

and a majority phase with the Fe vacancies ordered in different superlattice patterns¹⁰⁻¹³. The most commonly reported superlattice structure with Fe vacancy order is the $\sqrt{5} \times \sqrt{5} \times 1$ with space group $I4/m$ ^{5,6,14,15}. More recently, other superlattice patterns have been reported in the literature such as the $2 \times 2 \times 1$ ^{6,16}, the $1 \times 2 \times 1$ ^{6,7,16,17} and the $\sqrt{8} \times \sqrt{10} \times 1$ ⁸.

The distinction among the different superlattice patterns arises from the underlying order of the Fe and alkali metal sublattices. In the superstructure with space group $I4/m$, the Fe site symmetry is broken from the high temperature $I4/mmm$ space group, giving rise to two crystallographic sites. Preferred site occupancy leads to the $\sqrt{5} \times \sqrt{5}$ supercell, in which one site is empty (or sparsely occupied) while the other is almost full. Magnetic ordering is characteristic of this phase. Below $T_N \sim 560 \text{ K}$, AFM ordering arises in the $I4/m$ phase and persists well below T_c ⁵. The AFM magnetic state^{5,7,14} is robust unlike what has been reported in other Fe-based superconductors, and its coexistence with the superconducting state has raised concerns about the validity of the s+/- coupling mechanism coupled with the absence of hole pockets at the Fermi surface and the lack of nesting in this system¹⁸. More recently, evidence of alkali site vacancy order has been presented as well with a $\sqrt{2} \times \sqrt{2}$ superlattice structure within the $I4/mmm$ phase in $\text{K}_x\text{Fe}_{2-y}\text{Se}_2$ ¹⁰ and $\text{Cs}_x\text{Fe}_{2-y}\text{Se}_2$ ¹⁹⁻²¹. The centrosymmetry of the $I4/mmm$ is broken due to the alkali metal order. The $I4/mmm$ phase with no Fe vacancy has largely been attributed to be the host of superconductivity in part because of the absence of magnetism and vacancies.

It is understood at present that by post-annealing and quenching, superconductivity can be controlled in this system^{22,23} even though the actual mechanism remains unknown. Magnetic refinement from neutron powder diffraction measurements revealed that magnetic order does not exclude the presence of a SC phase²⁴. Moreover, a smaller magnetic moment was refined in NSC crystals indicating no correlation of the absence of mag-

netism and superconductivity. To identify which crystal phases are present, high-energy X-ray scattering measurements were performed on two kinds of $K_x\text{Fe}_{2-y}\text{Se}_2$ single crystals, one annealed and SC, and the other as-grown and NSC. In combination with Monte Carlo simulations, it is shown that superconductivity in the annealed and quenched crystal is most likely present in regions where the $\sqrt{5} \times \sqrt{5} \times 1$ Fe vacancy ordered I_4/m phase borders the I_4/mmm domains with no Fe vacancies. The in-between region consists of a non-magnetic Fe vacancy disorder phase. Thus superconductivity in this system appears at the crossover of the vacancy order-disorder transition. Quenching increases the boundary walls around the I_4/m domains, leading to an increase of the percolation paths and an enhancement of superconductivity.

Single crystals of $K_x\text{Fe}_{2-y}\text{Se}_2$ were grown using the self-flux method. The first step of the synthesis involved the preparation of high-purity FeSe by solid state reaction. Stoichiometric quantities of iron pieces (Alfa Aesar; 99.99%) and selenium powder (Alfa Aesar; 99.999%) were sealed in an evacuated quartz tube, and heated to 1075 °C for 30 hours, then annealed at 400 °C for 50 hours, and finally quenched in liquid nitrogen. In the second step, a potassium grain and FeSe powder with a nominal composition of $K:\text{FeSe} = 0.8:2$ were placed in an alumina crucible and double-sealed in a quartz tube back-filled with ultrahigh-purity argon gas. All samples were heated at 1030 °C for 2 hours, cooled down to 750 °C at a rate of 6 °/hr, and then cooled to room temperature by switching off the furnace. High quality single crystals were mechanically cleaved from the solid chunks. In the final step, the annealed crystals were additionally thermally treated at 350 °C under argon gas for 2 hours, followed by quenching in liquid nitrogen. The crystals that were not heat-treated were labeled as-grown. The magnetic susceptibility and transport were measured from 2 to 300 K and the as-grown crystal is NSC while the annealed crystal is SC. Back-scattered scanning electron microscopy (SEM) measurements were carried out at room temperature on the two samples²⁴. The characterization of these crystals was previously reported in Ref.²⁴. The SEM measurements showed that the surface morphology of the as-grown crystal has two kinds of regions: rectangular islands with a bright color and a background with a dark color. On the other hand, instead of island-like domains, very small bright dots were observed on the surface of the annealed crystal. Specific heat measurements performed on the SC crystals showed no transition at $T_C \sim 29$ K, as seen in Figs. 1 (e) and (f), indicating that it does not exhibit bulk superconductivity. The single crystal diffraction measurements were carried out at the Advanced Photon Source of Argonne National Laboratory, at the 11-ID-C beam line. In-plane and out-of-plane measurements were carried out on both types of crystals at room temperature.

The X-ray diffraction from the $hk0$ scattering plane shows evidence of coexistence of multiple phases, consist-

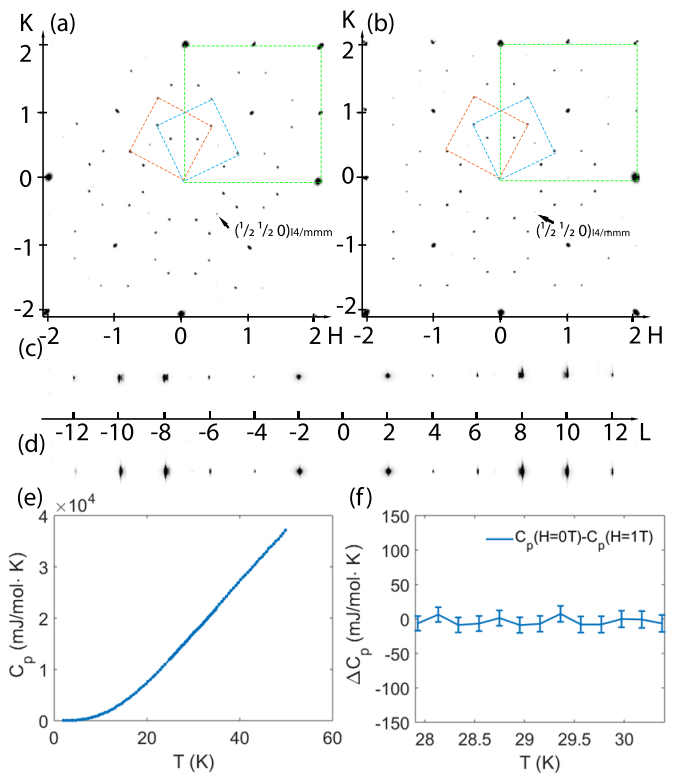


FIG. 1: The diffraction patterns from the $hk0$ plane from (a) as-grown and (b) quenched crystals. In (c) and (d) are the plots along the $00l$ direction in the as-grown and quenched crystal, respectively. The $hk0$ patterns consist of two configurations of the I_4/m phase highlighted by the two inner dashed boxes, and the I_4/mmm phase with a $\sqrt{2} \times \sqrt{2}$ superlattice structure highlighted by the outer dashed box. Subplot (e) shows the specific heat measurement of the SC sample at zero magnetic field (0 T). (f) is the difference of the SC sample's specific heat data at 0 T and 1 T in the vicinity of $T_c \sim 29$ K.

tent with earlier measurements. Shown in Figs. 1(a) and 1(b) are the patterns corresponding to the as-grown and quenched crystals, respectively. Several features are observed in both samples that arise from the presence of the two configurations of $\sqrt{5} \times \sqrt{5} \times 1$ superlattice structure with the I_4/m symmetry^{10,15} indicated by the two inner dashed boxes as well as the I_4/mmm phase indicated by the outer dashed box. The arrow points to a superlattice peak indexed to $(\frac{1}{2}, \frac{1}{2}, 0)$. The lattice constant calculated from this peak position matches that of the I_4/mmm phase with a $\sqrt{2} \times \sqrt{2}$ A-site vacancy order. The scattering patterns along the l -direction are shown in Figs. 1(c) and (d) for the as-grown and quenched crystals, respectively. Bragg peaks from I_4/mmm appear at the lower Q side of the I_4/m peaks. Neither $l=2n+1$ superlattice peaks nor diffuse scattering are observed along the $(00l)$ direction, leaving the out-of-plane stacking of the $\sqrt{2} \times \sqrt{2}$ K-vacancy order unclear. Due to sample rotation during measurement, weak reflections are observed at the lower Q and higher Q sides of the (006) and $(00\bar{6})$

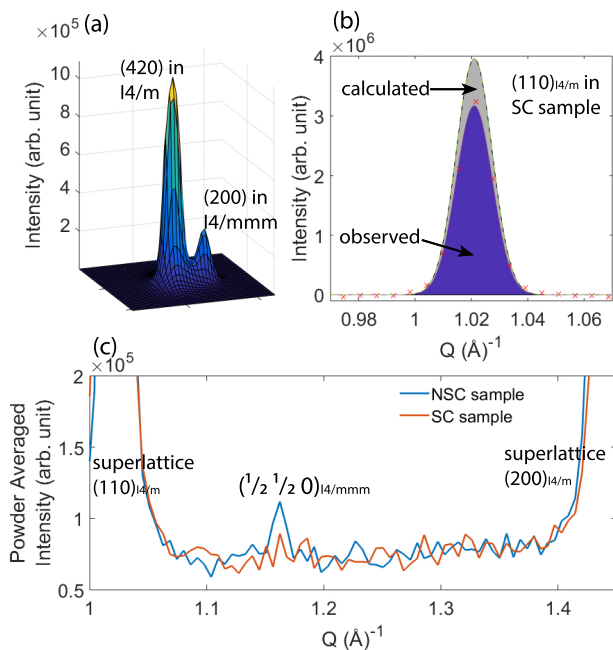


FIG. 2: (a) A comparison between Bragg peaks from I_4/m and I_4/mmm phases. (b) The observed superlattice peak (110) in SC crystal is compared with the calculated intensity based on an ideal I_4/m structure. (c) The powder integral of the $hk0$ scattering plane in the vicinity of the superlattice peak $(\frac{1}{2} \frac{1}{2} 0)$.

Bragg peaks, and can be indexed to the (204) and (206) Bragg peaks, respectively.

In both crystals, the diffraction pattern is dominated by a majority phase with the I_4/m space group with Fe vacancies and a minority phase consisting of the high symmetry I_4/mmm space group with no vacancies at the Fe site and a weak $\sqrt{2} \times \sqrt{2}$ vacancy order at the K site. Shown in Fig. 2(a) are the (200) Bragg peak from the I_4/mmm minority phase and the (420) Bragg peak from the I_4/m majority phase in the $hk0$ plane. They are well-resolved given that the two phases have different lattice constants ($a/\sqrt{5} \sim 3.90$ \AA in I_4/m , $a \sim 3.84$ \AA in I_4/mmm), often difficult to see in powders. Shown in Figs. 2(c) are the powder integrated diffraction patterns obtained from the annealed and as-grown crystals in the vicinity of the $(\frac{1}{2} \frac{1}{2} 0)$ superlattice peak. Even though this peak is observed in both diffraction patterns, it is significantly stronger and clearly above the background level in the as-grown crystal at $Q \sim 1.16$ \AA^{-1} but barely visible in the annealed sample. The $(\frac{1}{2} \frac{1}{2} 0)$ peak is not as intense as the other superlattice features which suggests that the K-site vacancy is partially ordered in the I_4/mmm phase. The K-site vacancy order can break the symmetry of the centrosymmetric I_4/mmm to P_4/mmm or to an even lower symmetry depending on its out-of-plane stacking pattern. However, our out-of-plane diffraction data did not provide enough information to further confirm the new symmetry. Single crystal refinement was performed

on the $hk0$ plane data, and the results are summarized in Tables I and II, where space group P_4/mmm was used to refine the $(\frac{1}{2} \frac{1}{2} 0)$ superlattice peak of the minority phase. How the K vacancy order affects superconductivity is still an open question. The refinement yielded a volume fraction for the I_4/mmm phase of 27(1)% in the annealed sample and about 33.5(6)% in the as-grown. At the same time, the refinement indicates that the I_4/m phase is not fully ordered with the $\sqrt{5} \times \sqrt{5} \times 1$ Fe vacancy ordered supercell (Appendix). Shown in Fig 2(b) is a comparison of the integrated intensity of the $(110)_{I_4/m}$ superlattice peak to the calculated intensity assuming a fully ordered Fe-vacancy. The experimental intensity is reduced which shows that even within the I_4/m majority phase, the Fe vacancies are not fully ordered. Two different Fe vacancy schemes are present within the I_4/m superstructure, one with fully ordered Fe vacancies and AFM order and one with partially ordered (or disordered) vacancies and non-magnetic. Focusing on the disordered Fe sublattice it is indistinguishable from the ordered Fe sublattice because their lattice constants are unresolved in the experimental data. The I_4/m phase evolves continuously from the high temperature I_4/mmm as shown by Ricci et al in Ref.¹⁰. The I_4/mmm was used to represent the Fe disordered sublattice. High pressure experiments are planned next to distinguish the Fe ordered from the Fe disordered sublattice.

The ordered and disordered Fe vacancy were modeled using a Monte Carlo (MC) simulation. The Hamiltonian was designed to be Ising like with the following form: $H = \sum_{\langle 21 \rangle} J_{21} \sigma_i \sigma_j + \sum_{\langle 31 \rangle} J_{31} \sigma_i \sigma_j + \sum_{\langle 11 \rangle} J_{11} \sigma_i \sigma_j + \sum_{\langle 20 \rangle} J_{20} \sigma_i \sigma_j + \sum_{\langle 22 \rangle} J_{22} \sigma_i \sigma_j$. Here the Ising variable $\sigma_i = 1$ represents an Fe atom at site i and $\sigma_i = -1$ stands for a vacancy at site i . The coupling constant between σ_i and σ_j were defined up to the 5th nearest neighbor. By setting $J_{11,20,22} > 0$, $J_{21,31} < 0$, the two $\sqrt{5} \times \sqrt{5}$ configurations will be energetically favored. For the Monte Carlo step, site swapping was employed instead of site flipping, in order to keep the vacancy ratio unchanged. When vacancies are less than 20 %, regions with no Fe vacancies will form on the lattice, simulating the I_4/mmm phase. The as-grown sample was simulated by gradually lowering the simulation temperature. Simulation of the annealed sample started from setting the temperature of the simulated as-grown lattice to a high temperature T_a till equilibrium, then set the temperature back down to base temperature. The simulation results of 15 % vacancies on a 300×300 lattice with $J_{11,20,22} = 6$, $J_{21,31} = -1.5$ and $T_a = 10$ are shown in Fig. 3. Before annealing, the two $\sqrt{5} \times \sqrt{5}$ configurations (blue and green) and the Fe vacancy free I_4/mmm phase (yellow) appear in big domains (Fig. 3(a)). After annealing, many small domains with the $\sqrt{5} \times \sqrt{5}$ structure form inside the previously vacancy free regions, breaking the I_4/mmm domains into smaller islands, creating more domain boundaries (Fig 3(b)). The simulated lattice is more homogeneous after the annealing process, in agreement with our SEM results²⁴. The volume ratio of the I_4/mmm phase also

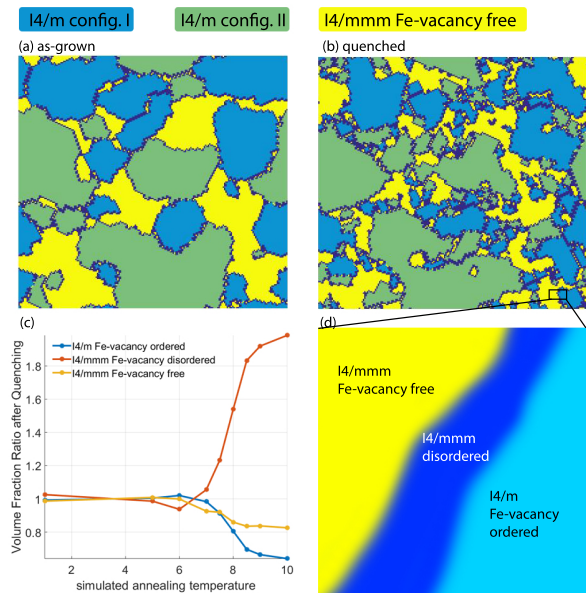


FIG. 3: (a) and (b) The phase distribution of the simulated lattice before and after simulated annealing and quenching processes. (c) The volume fraction ratio of each phases before and after quenching. (d) A schematic plot demonstrating the three phases.

decreases after annealing, which agrees with our X-ray data.

The annealing process controls the phase distribution in the MC as seen in Fig 3 (c). With annealing, the Fe disordered I_4/mmm phase grows significantly over the I_4/mmm Fe vacancy-free and I_4/m Fe vacancy-ordered phases. Difficult as it is to separate the contribution of the I_4/mmm disordered phase in the diffraction pattern, the difference between the experimental and calculated (110) superlattice peak intensities shown above in Fig 2(b) is an indication that the I_4/m is not fully ordered, consistent with the calculation. How does this affect superconductivity? Our Monte Carlo simulation indicates that the annealing process increases the total area of the domain boundary where Fe vacancies tend to be randomized. The increase in the domain boundary walls is seen in Fig 3(b). The length of the boundary walls increases as the domains get smaller. In a real sample this disorder can be enhanced by the local distortion at the domain boundaries due to different lattice constants of the two phases. It was previously shown using thin films of $K_x\text{Fe}_{2-y}\text{Se}_2$ ²⁵ that the superconducting phase appears when the I_4/mmm phase borders the I_4/m phase. The domain boundary forms a filamentary network of Fe vacancy disorder. The filamentary nature of SC is consistent with the Cp data. Fe vacancy disorder suppresses the band structure reconstruction and raises the chemical potential without completely destroying the Fermi surface²⁶. The Fe vacancy disorder can thus serve as effective doping and lead to superconductivity. This is consistent with our X-ray and simulation results and

TABLE I: Refined structure parameters for the I_4/m phase that includes both the Fe-vacancy disordered and Fe-vacancy ordered phases. Atomic position: K1, $2a$ (0,0,0); K2, $8h$ ($x, y, 0$); Fe1, $4d$ ($0, \frac{1}{2}, \frac{1}{4}$); Fe2, $16i$ ($x, y, 0.2515$); Se1, $4e$ ($\frac{1}{2}, \frac{1}{2}, 0.1351$); Se2, $16i$ ($x, y, 0.1462$). Out-of-plane coordinates are not refined, values are from ref⁵. If not listed, the site occupancy (Occ.) is 1.

		SC	NSC
	a (Å)	8.7261(7)	8.7243(5)
	c (Å)	14.108(4)	14.104(4)
K1	Occ.	0.75(7)	0.73(7)
	U_{iso}	0.046(7)	0.050(6)
	x	0.376(4)	0.377(2)
K2	y	0.196(2)	0.211(2)
	Occ.	0.73(7)	0.76(6)
	U_{iso}	0.046(7)	0.050(6)
Fe1	Occ.	-0.04(2)	-0.06(2)
	U_{iso}	0.016(3)	0.023(2)
Fe2	x	0.1990(4)	0.1979(3)
	y	0.0898(5)	0.0876(5)
	Occ.	0.90(2)	1.02(1)
Se1	U_{iso}	0.016(3)	0.023(2)
	U_{iso}	0.010(2)	0.018(1)
Se2	x	0.1070(4)	0.1083(3)
	y	0.3012(3)	0.3028(2)
	U_{iso}	0.010(2)	0.018(1)
wR		6.7%	5.0%
volume frac.		73(1)%	66.5(6)%

provides a connection to the transport properties of the two samples.

To conclude, the SC crystal has less of the I_4/mmm phase with no Fe vacancies than the NSC crystal. Furthermore, the simulation results indicate that the SC crystal tends to form more domain boundaries with the Fe-vacancy disordered phase sandwiched between the I_4/mmm vacancy free and the I_4/m vacancy ordered phases as seen in Fig 3(d), and very possibly leads to superconductivity in a filamentary form, in agreement with a reported SPEM study²⁷. The enhancement of superconductivity as well as the filamentary nature of the superconductivity in this compound is attributed to the increase of domain walls by annealing and quenching.

The authors would like to acknowledge valuable discussions with W. Bao, T. Egami, A. Bianconi, and W. Ku. The work at the University of Virginia is supported by the U. S. Department of Energy, Office of Basic Energy Science, DE-FG02-01ER45927.

*Corresponding author

E-mail: louca@virginia.edu

TABLE II: Refined structure parameters for the $P4/mmm$ Fe-vacancy free phase. Atomic position: K1, $1a$ $(0, 0, 0)$; K2, $2e$ $(\frac{1}{2}, 0, \frac{1}{2})$; K3, $1c$ $(\frac{1}{2}, \frac{1}{2}, 0)$; Fe1, $8r$ $(x, x, 0.25)$; Se1, $2g$ $(0, 0, 0.1456)$; Se2, $2h$ $(\frac{1}{2}, \frac{1}{2}, 0.1456)$; Se3, $4i$ $(0, \frac{1}{2}, 0.3544)$. Out-of-plane coordinates are not refined, values are from ref⁵. If not listed, the site occupancy (Occ.) is 1.

		SC	NSC
	$a(\text{\AA})$	5.437(1)	5.433(1)
	$c(\text{\AA})$	14.230(7)	14.237(2)
K1, K2	U_{iso}	0.03(1)	0.068(4)
K3	Occ.	0.47(5)	0.52(1)
	U_{iso}	0.03(1)	0.068(4)
Fe1	x	0.249(1)	0.244(1)
	U_{iso}	0.039(5)	0.023(1)
Se1, Se2, Se3	U_{iso}	0.023(3)	0.029(1)
wR		6.1%	1.4%
volume frac.		27(1)%	33.5(6)%

I. APPENDIX

The X-ray diffraction data from 11-ID-C, Advanced Photon Source of Argonne National Laboratory were collected in the form of intensity per pixel on the area detector during sample rotation. To obtain the structure factor from the data for single crystal Rietveld refinement, three important scale factors have to be removed from the data.

The first scale factor is from the polarization of the X-ray beam. The electric field component parallel to the scattered wave vector cannot travel to the detector as radiation. Thus for X-rays polarized parallel to the scattering plane (the plane defined by the incident and scattered wave vectors), the intensity radiated to the detector is reduced by a factor of $\cos^2(2\theta)$ comparing to X-ray polarized perpendicular to the scattering plane. 11-ID-C uses unpolarized beam, so the scale factor becomes $(1 + \cos^2(2\theta))/2$.

The second scale factor, $\sin^{-1}(2\theta)$, comes from the *Jacobian* of the basis change from an angular basis in real

space to the reciprocal lattice basis. Derivation can be found in X-Ray Diffraction by B. E. Warren.²⁸

The third one depends on the angle between \vec{G}_{hkl} and the sample rotation axis, i.e. ϕ_{hkl} . When the sample rotates by $d\alpha$, \vec{G}_{hkl} rotates by $\sin(\phi_{hkl})d\alpha$ accordingly. This leads to a scale factor of $1/\sin(\phi_{hkl})$ in the collected diffraction pattern. Removing it requires finding the rotation axis. This is achieved by taking the ratio between integrated intensity of same hkl reflections from the two configurations of $I4/m$ phase. The structure factor cancels out, and the intensity ratio is proportional to the ratio of the scale factor and volume fraction of the two configurations, as shown in the following equation.

$$\frac{I_{hkl,1}}{I_{hkl,2}} \propto \frac{V_1}{V_2} \cdot \frac{\sin(\phi_0 + \varphi_{hkl,2})}{\sin(\phi_0 + \varphi_{hkl,1})} \quad (1)$$

Here the subscript 1 and 2 represent the two configurations. ϕ_0 defines the direction of the rotation axis. By tuning the angle ϕ_0 , the best fitting on the reflections in HK0 plane is reached at $\phi_0 = -2.1^\circ$ with $Rsq = 0.97$.

The structure factor of reflections in the hk0 plane were obtained by integrating the peak intensity, removing the above scale factors then taking the square root. The two configurations of $I4/m$ were combined into one $I4/m$ phase. Single crystal refinement results based on these structure factors are listed in Table I and II. In the NSC sample, the Fe site occupancies are close to a perfect $\sqrt{5} \times \sqrt{5}$ vacancy order. On the other hand in the SC sample, the Fe2 site has an occupancy of 0.90(2), while the Fe1 site is almost empty. The partially occupied Fe2 site indicates partial order of the Fe vacancy. But the occupancy of Fe1 site does not agree well with that. The correlation between occupancy and thermal factor is particularly strong when the site is almost empty. Therefore the refinement result of Fe2 occupancy is more reliable than the Fe1 occupancy. It is difficult to quantify the degree of partial order in the SC sample, but the different Fe2 occupancy clearly demonstrates that the annealed and quenched SC sample has vacancy disorder in the $I4/m$ phase whereas the as-grown NSC sample does not.

¹ S. Kasahara, H. J. Shi, K. Hashimoto, S. Tonegawa, Y. Mizukami, T. Shibauchi, K. Sugimoto, T. Fukuda, T. Terashima, Andriy H. Nevidomskyy & Y. Matsuda, Nature **486**, 382 (2012).

² P. Dai, J. Hu & E. Dagotto, Nat. Phys. **8**, 709 (2012) and references therein.

³ G. Campi, A. Bianconi, N. Poccia, G. Bianconi, L. Barba, G. Arrighetti, D. Innocenti, J. Karpinski, N. D. Zhigadlo, S. M. Kazakov, M. Burghammer, M. v. Zimmermann, M. Sprung & A. Ricci, Nature **525**, 359 (2015).

⁴ J. Guo, S. Jin, G. Wang, S. Wang, K. Zhu, T. Zhou, M. He, & X. Chen, Phys. Rev. B, **82**, 180520(R) (2010).

⁵ Bao Wei, Huang Qing-Zhen, Chen Gen-Fu, M. A. Green, Wang Du-Ming, He Jun-Bao & Qiu Yi-Ming, Chin. Phys. Lett. **28**, 086104 (2011).

⁶ Bao Wei, Li Guan-Nan, Huang Qing-Zhen, Chen Gen-Fu, He Jun-Bao, Wang Du-Ming, M. A. Green, Qiu Yi-Ming, Luo Jian-Lin & Wu Mei-Mei, Chin. Phys. Lett. **30**, 027402 (2013).

⁷ Y. J. Yan, M. Zhang, A. F. Wang, J. J. Ying, Z. Y. Li, W. Qin, X. G. Luo, J. Q. Li, Jiangping Hu & X. H. Chen, Sci. Rep. **2**, 212 (2012).

⁸ Xiaxin Ding, Delong Fang, Zhenyu Wang, Huan Yang, Jianzhong Liu, Qiang Deng, Guobin Ma, Chong Meng,

- Yuhui Hu & Hai-Hu Wen, *Nat. Commun.* **4**, 1897 (2013)
- ⁹ Scott V. Carr, Despina Louca, Joan Siewenie, Q. Huang, Aifeng Wang, Xianhui Chen, & Pengcheng Dai, *Phys. Rev. B* **89**, 134509 (2014)
- ¹⁰ A. Ricci, N. Poccia, B. Joseph, G. Arrighetti, L. Barba, J. Plaisier, G. Campi, Y. Mizuguchi, H. Takeya, Y. Takano, N. L. Saini & A. Bianconi, *Supercond. Sci. Technol.* **24**, 082002 (2011)
- ¹¹ A. Ricci, N. Poccia, G. Campi, B. Joseph, G. Arrighetti, L. Barba, M. Reynolds, M. Burghammer, H. Takeya, Y. Mizuguchi, Y. Takano, M. Colapietro, N. L. Saini, & A. Bianconi, *Phys. Rev. B* **84**, 060511(R) (2011)
- ¹² Wei Li, Hao Ding, Peng Deng, Kai Chang, Canli Song, Ke He, Lili Wang, Xucun Ma, Jiang-Ping Hu, Xi Chen & Qi-Kun Xue, *Nature Physics* **8**, 126-130 (2012)
- ¹³ R. H. Yuan, T. Dong, Y. J. Song, P. Zheng, G. F. Chen, J. P. Hu, J. Q. Li & N. L. Wang, *Sci. Rep.* **2**, 221 (2012)
- ¹⁴ F. Ye, S. Chi, Wei Bao, X. F. Wang, J. J. Ying, X. H. Chen, H. D. Wang, C. H. Dong, & Minghu Fang, *Phys. Rev. Lett.* **107**, 137003 (2011).
- ¹⁵ P. Zavalij, Wei Bao, X. F. Wang, J. J. Ying, X. H. Chen, D. M. Wang, J. B. He, X. Q. Wang, G. F. Chen, P.-Y. Hsieh, Q. Huang, & M. A. Green, *Phys. Rev. B.* **83**, 132509 (2011).
- ¹⁶ Z. Wang, Y. J. Song, H. L. Shi, Z. W. Wang, Z. Chen, H. F. Tian, G. F. Chen, J. G. Guo, H. X. Yang, & J. Q. Li, *Phys. Rev. B.* **83**, 140505(R) (2011).
- ¹⁷ S. M. Kazakov, A. M. Abakumov, S. Gonzalez, J. M. Perez-Mato, A. V. Ovchinnikov, M. V. Roslova, A. I. Boltalin, I. V. Morozov, E. V. Antipov, & G. Van Tendeloo, *Chem. Mater.* **23**, 4311 (2011).
- ¹⁸ Y. Zhang, L. X. Yang, M. Xu, Z. R. Ye, F. Chen, C. He, H. C. Xu, J. Jiang, B. P. Xie, J. J. Ying, X. F. Wang, X. H. Chen, J. P. Hu, M. Matsunami, S. Kimura & D. L. Feng, *Nat. Mater.* **10**, 273 (2011)
- ¹⁹ A. Bosak, V. Svitlyk, A. Krzton-Maziopa, E. Pomjakushina, K. Conder, V. Pomjakushin, A. Popov, D. de Sanctis, & D. Chernyshov, *Phys. Rev. B* **86**, 174107 (2012)
- ²⁰ K. M. Taddei, M. Sturza, D. Y. Chung, H. B. Cao, H. Claus, M. G. Kanatzidis, R. Osborn, S. Rosenkranz, & O. Chmaissem, *Phys. Rev. B* **92**, 094505 (2015)
- ²¹ D. G. Porter, E. Cemal, D. J. Voneshen, K. Refson, M. J. Gutmann, A. Bombardi, A. T. Boothroyd, A. Krzton-Maziopa, E. Pomjakushina, K. Conder, & J. P. Goff, *Phys. Rev. B* **91**, 144114 (2015)
- ²² F. Han, H. Yang, B. Shen, Z.-Y. Wang, C.-H. Li & H.-H. Wen, *Philos. Mag.* **92**, 2553 (2012).
- ²³ H. Ryu, H. Lei, A. I. Frenkel, & C. Petrovic, *Phys. Rev. B* **85**, 224515 (2012).
- ²⁴ J. Yang, C. Duan, Q. Huang, C. Brown, J. Neuefeind, & D. Louca, *Phys. Rev. B* **94**, 024503 (2016).
- ²⁵ W. Li, H. Ding, Z. Li, P. Deng, K. Chang, K. He, S. Ji, L. Wang, X. Ma, J.-P. Hu, X. Chen, & Q.-K. Xue, *Phys. Rev. Lett.* **109**, 057003 (2012).
- ²⁶ T. Berlijn, P. J. Hirschfeld, & W. Ku, *Phys. Rev. Lett.* **109**, 147003 (2012).
- ²⁷ M. Bendele, A. Barinov, B. Joseph, D. Innocenti, A. Iadecola, A. Bianconi, H. Takeya, Y. Mizuguchi, Y. Takano, T. Noji, T. Hatakeda, Y. Koike, M. Horio, A. Fujimori, D. Ootsuki, T. Mizokawa & N. L. Saini, *Sci. Rep.* **4**, 5592(2014).
- ²⁸ B. E. Warren, *X-Ray Diffraction*. Addison-Wesley, Reading, MA. (1969).